A Computational Intelligence Characterization of Solar Magnetograms

Julio J. Valdés
Digital Technologies Research Centre
National Research Council Canada
Ottawa, Canada
julio.valdes@nrc-cnrc.gc.ca

Ljubomir Nikolić
Canadian Hazards Information Service
Natural Resources Canada
Ottawa, Canada
ljubomir.nikolic@canada.ca

Simone Disabato
Dip. di Elettronica, Informazione e Bioingegneria
Politecnico di Milano
Milano, Italy
simone.disabato@polimi.it

Manual Roveri
Dip. di Elettronica, Informazione e Bioingegneria
Politecnico di Milano
Milano, Italy
manuel.roveri@polimi.it

***Abstract*—Space Weather (SW) poses a hazard to modern society. SW phenomena depend on the Sun's magnetic field and understanding and forecasting the solar magnetic field is an important research subject. To achieve this goal, in this paper Global Oscillation Network Group (GONG) solar magnetograms 2006-2019 are investigated with different approaches provided by unsupervised and supervised Computational Intelligence techniques. Such techniques were successful at providing insights into the behavior and evolution of the photospheric magnetic field, revealing patterns of activity and their relation with the different phases of the solar cycle. On the one hand, representative prototypes of synoptic maps were found, capturing the variations in homogeneity, intensity and variability of magnetic activity. On the other hand, Convolutional neural networks combined with transfer learning and dimensionality reduction techniques were helpful in providing classification models which accurately predict classes associated to the main stages of the cycle. Such models provide results in good correspondence with the natural classes found in feature spaces and have classification errors concentrated mostly at transition periods of the solar cycles.**

***Index Terms*—Space weather, solar synoptic maps, computational intelligence, MSSIM image similarity, intrinsic dimension, clustering (optics, pam, kmeans), low dimensional mappings, deep learning, convolutional neural networks, transfer learning, svm.**

I. Introduction

Space Weather (SW) represents a chain of processes that begin at the Sun. They can adversely affect technology on Earth and pose hazards to modern society. For these reasons, significant research efforts are undertaken to understand and forecast SW and its impacts on Earth activities. More specifically, the complex interplay between plasma and magnetic field is the source of solar disturbances such as solar flares and Coronal Mass Ejections (CME). Since the magnetic field controls the solar outputs, information about the magnetic field is widely used in research and operational SW models. Although regular space and ground based measurements of the Sun's magnetic field are available, they are restricted to the side of the Sun facing the Earth (near side) and to the photosheric/chromspheric heights [22]. At these heights, close to the surface of the Sun, the plasma density is high enough for a favorable signal-to-noise ratio. The noise level represents a significant challenge for measurements on the limbs of the solar disc, which is the visible surface of the Sun. Furthermore, due to the approximately 7.25 degree tilt of the Sun's rotation axis in respect to the ecliptic plane, the polar regions are not always visible and different techniques are used to fill the gaps in the polar regions [28].

SW has many unanswered questions about physical processes and significant gaps still exists. Due to the fact that a significant amount of solar observations exists in the solar and SW community, Machine Learning (ML) could be a viable solution to provide significant scientific and application advances. Such ML techniques aim at examining the behavior and determining the evolution of the Sun's magnetic field. Since measurements of the field are restricted to the near side, there is an interest to predict active regions on the far side of the Sun. This is particularly important for SW forecasting since, as the Sun rotates, these regions emerge on the near side where associated solar disturbances are more geoeffective.

This paper uses machine and deep learning techniques from Computational Intelligence (CI) techniques to study and characterize the behavior of the Sun's magnetic field. To achieve this goal we relied on magnetic field data from the Global Oscillation Network Group (GONG) observations [14]. GONG provides solar magnetograms of the photospheric magnetic field with 24 h coverage of the Sun. These data are widely used in the research and operational SW community. For example, GONG synoptic maps are used with numerical models to derive the coronal magnetic field [20], [21], and to forecast CME propagation and arrival times [27], [23].

The paper is organized as follows. In Sections II and III, solar magnetograms, GONG synoptic maps and data preprocessing are described. The machine and deep learning CI techniques employed for magnetograms characterization are

978-1-7281-6926-2/20/$31.00 ©2020 Crown

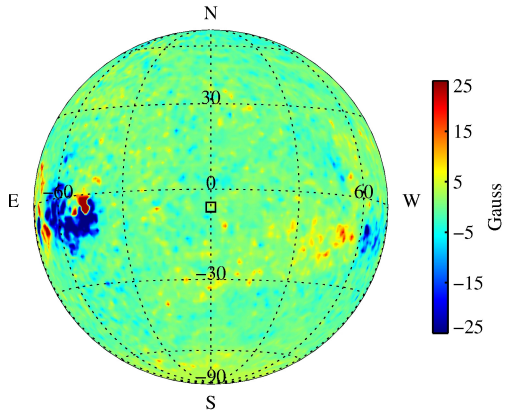

Fig. 1. Photospheric magnetic field of the Sun as viewed from the Earth on January 29, 2007 (05:54 UT). The field is saturated at ±25 Gauss. E, W, N and S denote East, West, North and South, respectively. The small square in the image represents the projection of the Earth on the solar disc.

described in Sections IV and V respectively. The results of the work are presented in Section VI and the conclusions are given in Section VII.

II. Solar Magnetograms

A solar magnetogram represents an image of the magnetic field on the solar disc. To illustrate, in Figure 1 we show the GONG solar magnetogram of the photospheric magnetic field for January 29, 2007 (05:54 UT). Here, we use zeropoint corrected data ("mrzqs" and the UT timestamp in the filename) from the GONG archive (https://gong.nso.edu). The red and blue color represent the magnetic field directed away from and towards the Sun, respectively. The field in Figure 1 represents the radial component of the magnetic field $B_r(R_0, \theta, \phi)$, where, R_O is the radius of the Sun, θ is the colatitude, and ϕ is the longitude. In the figure a region with a strong magnetic field is visible on the East limb of the solar disc. As the Sun rotates, with about 27.27 day rotation period, this active region will move from East (E) to West (W) and cross the central meridian. The solar magnetograms can be combined into so-called synoptic maps which are often used in SW research and operations [14]. These maps that represent full surface maps of the Sun's magnetic field will be detailed in the next section.

III. Synoptic Maps and Data Preprocessing

In this paper we use re-meshed GONG synoptic maps S (organized as matrix $[s_{\theta,\phi} = B_r(R_0, \theta, \phi)]$), with uniform 1° resolution in θ and ϕ. These re-meshed maps improve the accuracy of the widely used potential field source surface model of the solar corona, particularly spherical harmonics in the polar regions [29], [20].

Figure 2 shows two examples of re-meshed synoptic maps S, for (a) January 29, 2007 (05:54 UT), and (b) September 6, 2014 (17:04 UT). The map time is associated with the central meridian that is denoted with the dash-dash line, while the dash-dot line denotes projections of the Earth on the map at different times. As the Sun rotates, the region $\phi < -60^\circ$ will

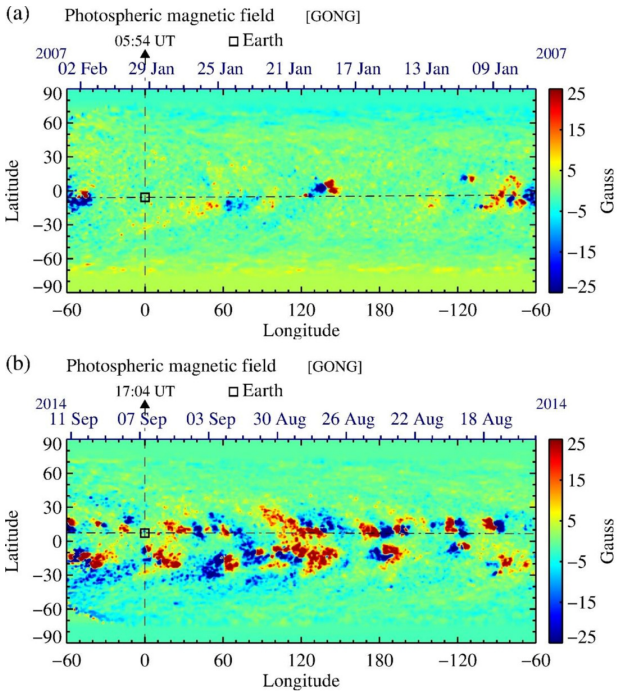

Fig. 2. GONG synoptic maps of the photospheric magnetic field for (a) January 29, 2007 (05:54 UT) and (b) September 06, 2014 (17:04 UT). The magnetic field is saturated at ±25 Gauss. The central meridian and sub-Earth locations are denoted with dash-dash and dash-dot line, respectively.

cross the central meridian. The synoptic map in Figure 2a corresponds to the solar magnetogram from Figure 1, and illustrates the magnetic field of the Sun close to the solar cycle 23 minimum, while Figure 2b shows the field around the maximum of solar cycle 24.

The GONG synoptic maps are assembled from many measurements of the photospheric magnetic field, including measurements from different observatories to provide daily coverage of the Sun. All those measurements are weighted when computing the synoptic map. Since a particular measurement can capture only the field on the near side of the Sun, the far side on the synoptic map consists of non-updated, past data. Furthermore, due to the limb noise, only the longitudinal region $-60^\circ < \phi < -60^\circ$ most accurately captures the Sun's magnetic field.

Summing up, in this paper we consider synoptic maps $S \in \mathbb{R}^{\Theta \times \Phi}$, where $\Theta = 181$ and $\Phi = 360$. We use two maps per day, from November 1, 2006, to September 30, 2019, typically obtained at 05:04 and 17:04 UT. When the maps are not available at those times, the closest ones are used if the time difference is less than two hours. There are some days when no map is available in the GONG archive.

To be used as input for the deep learning solutions proposed in Section V, the maps are converted to images by assigning a three-dimensional color (from any perceptual uniform colormap) in the interval $[-100, 100]$. All the values out of this interval are considered as the nearest value of the interval, i.e., -100 for negative values and 100 for positive ones.

IV. Machine Learning Techniques for Solar Magnetograms Characterization

The machine learning analysis of solar magnetograms has two main goals. First a low-dimensional representation is found (Sections IV-A to IV-C). After that, in Section IV-D, clustering methods are employed to study the data structures in this new representation.

A. Similarity Measures (MSSIM)

In this paper, the similarity between two solar magnetograms S_1 and S_2 is estimated with the Mean Structural Similarity Index (MSSIM) [10], which is a state-of-the-art perception-based method able to detect changes in the data structural information and it has been proven to capture the *human* notion of image similarity [6], [34]. It is computed by averaging the Structural Similarity Index (SSIM) on M low-pass filtered versions $S^{(j)}$ of the original image (here, a solar magnetogram), with M filters of different sizes, i.e.:

$$MSSIM\left(S_1, S_2\right) = \frac{1}{M}\sum_{j=1}^{M} SSIM\left(S_1^{(j)}, S_2^{(j)}\right) \quad (1)$$

The SSIM is then computed as follows:

$$SSIM\left(S_1, S_2\right) = \frac{(2\cdot\mu_1\cdot\mu_2 + C_1)\cdot(2\cdot\sigma_{12} + C_2)}{(\mu_1^2\cdot\mu_2^2 + C_1)\cdot(\sigma_1^2\cdot\sigma_2^2 + C_2)} \quad (2)$$

where S_1 and S_2 are two magnetograms, C_1 and C_2 are two regularization constants, $\mu_1, \sigma_1, \mu_2, \sigma_2$ are the means μ and the standard deviations σ of S_1 and S_2, respectively, and σ_{12} the correlation coefficient of S_1 and S_2.

Finally, the notion of MSSIM dissimilarity ($dMSSIM$) is derived as the complement of the MSSIM similarity:

$$dMSSIM\left(S_1, S_2\right) = 1 - MSSIM\left(S_1, S_2\right) \quad (3)$$

B. Intrinsic Dimension

Independently from the way the data are represented, either in a descriptor space or by a structure of pairwise dissimilarities, the data might be concentrated in low-dimensional manifolds. The goal of *intrinsic dimension* analysis is to find the dimensionality of such manifolds, to better understand the data structure and, in turn, improve the learning ability of machine learning models [32]. The solar magnetograms are here represented by a structure of pairwise $dMSSIM$ dissimilarities (defined in Eq. (3)), and the intrinsic dimension estimation is performed with the following four methods: the maximum likelihood estimator (MLE) [17]; the correlation integral [12]; the Nearest Neighbour estimator [30], [32]; and the U-statistic [13].

C. Low-Dimensional Spaces for Data Exploration

Once the intrinsic dimension has been estimated, techniques to represent the data in low dimensional spaces are needed. In this paper, we focus on transformations that preserve the local distances/dissimilarities or the conditional probability distributions within neighbourhoods in the higher and lower dimension spaces, i.e., the Sammon nonlinear mapping [24] and the t-Distributed Stochastic Neighbor Embedding (t-SNE) [15].

More specifically, the Sammon nonlinear mapping [24] preserves the local dissimilarities by minimizing the following error function:

$$S_e = \frac{1}{\sum_{i<j}\delta_{ij}^*}\sum_{i<j}\frac{(\delta_{ij}^* - d_{ij})^2}{\delta_{ij}^*} \quad (4)$$

where δ_{ij}^* denotes the dissimilarity between two objects in the original space and d_{ij} the distance in the projected space (Euclidean in our case).

In t-SNE [15], the mapping to a lower dimensional space is formulated in terms of matching conditional probability distributions between the original and the target spaces. Defined as $p_{j|i}$ the probability of an object x_i to be a neighbour of x_j, we have:

$$p_{j|i} = \frac{exp(-\|x_i - x_j\|^2/2\sigma_i^2)}{\sum_{k\neq i} exp(-\|x_i - x_k\|^2/2\sigma_i^2)} \quad (5)$$

where σ_i^2 is the variance around object x_i and k is a parameter (perplexity), related to local neighbors sizes.

Both transformations (Eqs. (4) and (5)), use the dMSSIM dissimilarity (Eq. (3)) as δ^* and $\|$ respectively. We also emphasize that, in our case, the objects xs of the two transformations are the magnetograms.

D. Clustering

Clustering methods are used for investigating the structure of the data from an unsupervised perspective. In particular, Optics [8] and k-Medoids (PAM) [16] were used.

More specifically, Ordering Points to Identify Cluster Structure (Optics) [8] is a density-based clustering method. The number of clusters is not specified a priori, and the algorithm finds the clusters by identifying regions with high-density, given the maximum distance ϵ at which to look for neighbours and the minimum number N of samples to define a cluster. In Optics, a rechability distance metric is introduced between two points x_i and x_j (in our case the magnetograms) and it is defined as the maximum between the core distances of x_i and the distance between x_i and x_j, where the core distance is the distance between x_i and the N-th farthest point in the N_ϵ neighbourhood of x_i. The core distance is undefined if the point x_p has not N neighbours within the distance ϵ. The reachability distance defines an ordering of points such that clusters are identified as valley regions in the reachability function (a plot of the reachability distance vs. the point reordering).

The Partitioning Around Medoids (PAM) technique [16], [25] aims at dividing the data into a given number of clusters, similarly to the k-Means algorithm [19]. However, it is more robust to the presence of outliers, and produces *medoids* which are prototype objects (cluster representatives) for which the average dissimilarity w.r.t. all other cluster members is minimal[1].

[1]The sum of intra-clusters dissimilarities is the cost function of the PAM algorithm.

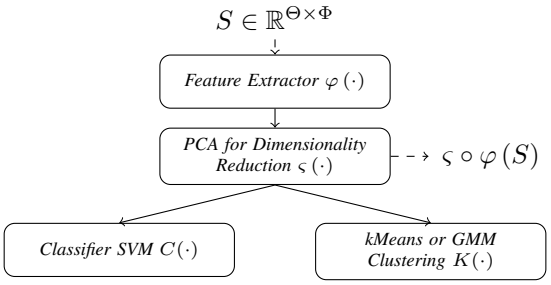

Fig. 3. The proposed deep learning architecture to characterize solar magnetograms Ss. On the extracted features $\varsigma \circ \varphi(S)$, various supervised or unsupervised techniques can be applied.

V. Deep Learning Solutions to Characterize Solar Magnetograms

A. Solar Activity Classes Definition

The solar activity within solar cycle 24 has been divided into four (unbalanced) classes, trying to respect as much as possible the physical structure of the problem, starting from what described by Schwabe [26]:

- *Low* (794 magnetograms): the initial period of a solar cycle, characterized by low solar activity. In our cases, the *low* activity period start from the beginning of cycle 24, estimated in December 2008 up to the end of 2009;
- *Rising* (848): after the *low* activity phase, a small transition period to the *high* activity one exists, here considered as a standalone class. It covers the period from January, 1 2010 to the end of February 2011;
- *High* (2866): this is the phase of the solar cycle characterized by the highest solar activity and, the highest solar disturbances. It covers the period from March 1, 2011 to January 31, 2015;
- *Decline* (3406): after the *high* activity phase, the solar activity declines up to the next solar cycle. This period covers the magnetograms from February 2015 to the last available ones in the series[2].

It is noteworthy to point out that the crisp boundaries between these phases are artificially introduced, while in real world situations they are smooth. For this reasons, classification errors close to such boundaries are reasonably expected (since most classification algorithms assume sharp boundaries). The definition of classes is shown in Figure 10b, together with the 10.7 cm solar radio flux that is an indicator of solar activity [18], [31].

B. Deep Learning Solutions

The pre-processed solar magnetograms S are converted to images, where each color corresponds to a magnetic field value in the $[-100, 100]$ interval. Such images are processed by a suitable defined deep learning solution, whose architecture described in Figure 3. In particular, the solution comprises the following steps:

[2]The end of solar cycle 24 is indeed estimated to be in late 2019.

TABLE I
Intrinsic Dimension estimation with different approaches.

Estimator	Value
Correlation Integral [12]	5.73
Maximum Likelihood Estimation [17]	4.53
Nearest Neighbor Information [30], [32]	5.45
Convergence Property of U-stats [13]	3

- a pre-trained Convolutional Neural Network (CNN) $\varphi(\cdot)$ acting as a feature extractor following a *transfer learning* approach [7], [33]. We relied on transfer learning since since in CNNs the first layers tipically extract general and common features, such as the color blobs, edges and corners, whereas deeper ones extract application specific features [33]. Hence, as done in [1], [3], the feature extractor φ considered here is general enough to extract the features for the subsequent processing.
- a dimensionality reduction operator $\varsigma(\cdot)$. This step is crucial to mitigate the *curse of dimensionality* problem deriving from high-dimensional spaces that typically characterize CNNs [11]. In this work we used Principal Component Analysis [9] as feature extractor operator. The feature space defined by $\varsigma \circ \varphi(\cdot)$ represents solar magnetograms S in the reduced space of CNNs.
- Finally, the reduced feature vector can be processed by both supervised and unsupervised ML techniques. In this paper, we focus on Support Vector Machines [2] as supervised, and on k-Means [19] and Gaussian Mixture Models as unsupervised clustering techniques. More specifically, the supervised classification is meant to recognize the solar activity classes defined in Section V-A, whereas clustering techniques should validate the definition of these classes by identifying clusters that match them (ideally, each cluster should contain samples belonging to only one class).

We emphasize that the proposed deep learning architecture does not require training, except for the computation of the PCA ς. However, nothing avoid to refine the feature extractor φ, for example, with some solar magnetogram images Ss.

VI. Results

A. Machine Learning Analysis

The results obtained with Optics and PAM clustering in the original magnetograms space are shown in Figure 4. Optics clustering (with $\epsilon = 1$ and $N = 14$) exhibits a very sharp drop in the reachability distance (Figure 4a), indicating the presence of two major clusters, in turn subdivided into higher and lower density areas, as evidenced by inflection points 3300 and 8900 in the reordered object axis of the reachability function. The estimates of intrinsic dimension for the $dMSSIM$ dissimilarity matrix are shown in Table I for all the considered methods. Interestingly, most estimates place the intrinsic dimension in the $[5, 6]$ interval, indicating that even though the dimensionality is not excessively high, it is larger

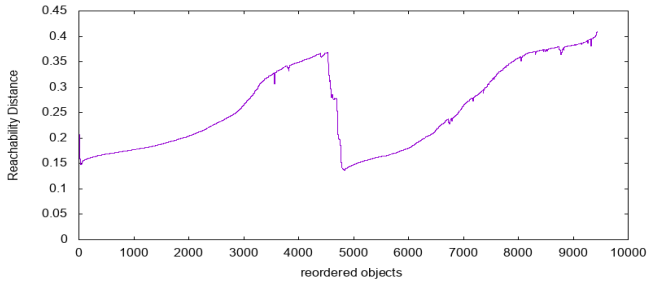

(a) Optics clustering. It shows two main and two smaller clusters.

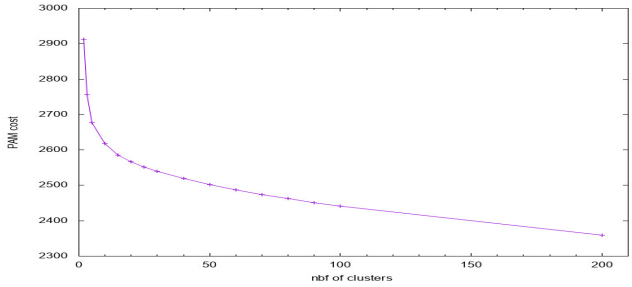

(b) PAM clustering. It exhibits an elbow at $k = 10$ medoids.

Fig. 4. Clustering results.

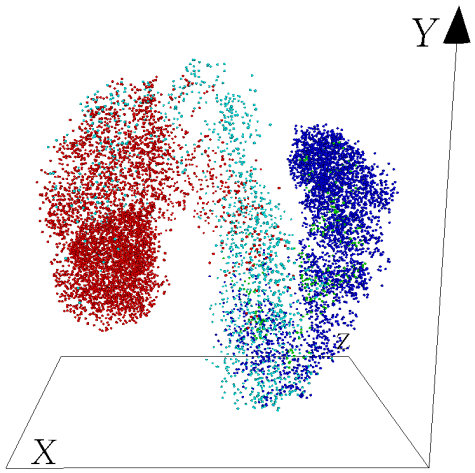

(a) Sammon mapping with overlaid Optics clusters.

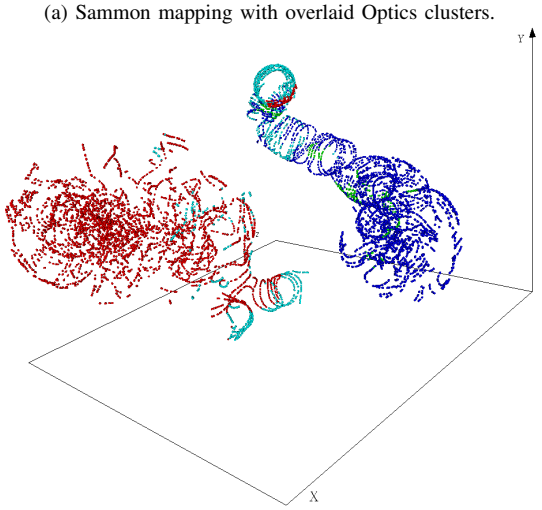

(b) t-SNE mapping with overlaid Optics clusters.

Fig. 5. Sammon and t-SNE mappings with overlaid Optics clusters.

than 3. Accordingly, the nonlinear mapping of the dissimilarity information to 3D spaces should be taken as an approximation, useful for orientation purposes.

The low-dimensional mappings obtained with the Sammon and the t-SNE techniques are presented in Figure 5. Optics cluster memberships are not used when computing the mappings and are overlaid in Fig. 5 for comparison purposes. The higher density regions within the red and blue classes correspond to the start and decline of the solar cycle (comprising 4527 and 3340 objects, respectively), while the cyan and green classes correspond to the middle part of the cycle (comprising 1294 and 273 objects, respectively) that are typically associated to the states of higher intensity and variability in magnetic activity. The t-SNE space clearly illustrates the association of the drop in reachability with the onset of the high magnetic activity period (the large discontinuity at the center of Figure 5b), as well as the more oscillatory behavior of the process, indicated by the spiraling pattern of the objects in the cyan class and part of the blue class. As the cycle starts to decline, the spiraling pattern in the blue class fades and almost disappears at the end of the cycle (the higher density region of the blue class at the lower-right in Figure 5b).

The behaviour of PAM's clustering cost function (described in Section IV-D) w.r.t. the number of medoids is shown in Figure 4b. The elbow at 10 medoids suggests the appropriate number of clusters. The medoids are represented in Figure 6 on the Sammon mapping, with spheres proportional to the cluster size. The vector polyline joining the clusters indicate the time evolution, mostly associated to the negative X axis (from left to right on Figure 6), despite the difference between the intrinsic dimension of the data and the 3D representation. Finally, the bigger clusters (and thus similarity among members) lie at the beginning and end of the cycle, indicating a larger variability in the high activity phases of the cycle itself.

B. Deep Learning Analysis

1) Implementation: The architecture, detailed in Section V, has been implemented in Python (PyTorch). In particular, two CNNs have been considered for the feature extractor φ: the AlexNet [4] at the end of each convolutional block (precisely, the pooling layer at the first, second, and fifth block, the Relu non linearities at the others), and the ResNet-101 [5] after each of the 32 residual blocks. The PCA ς are computed, in each case, on the number of components that keep the 95% of the variance. Finally, the seed has been fixed in all experiments, for homogeneity and reproducibility.

2) Results: The classification results for the considered CNNs are shown in Figure 9, with a 50-50% training/testing split of the solar magnetograms. The AlexNet (Figure 9a) shows an extremely high accuracy on the *High* activity class as well as some difficulties with the other classes, especially the *Rising* one. The fourth layer (*relu4*) exhibits the best performances on all classes with a global accuracy of 0.925,

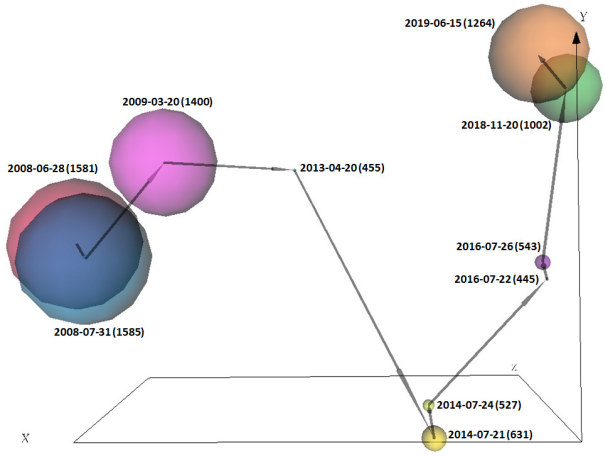

Fig. 6. Sammon mapping with overlaid 10 medoids.

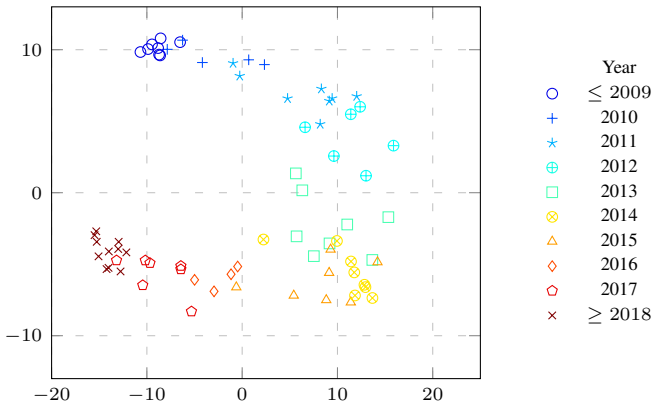

Fig. 7. Time distribution on the first two PCs of the feature space.

whereas the fifth layer (*pool5*) has a very low accuracy on the *Low* class, despite comparable or better performances on other classes w.r.t. *relu4* layer. The first eight ResNet layers show a low accuracy for the Low class, whereas the last layer exhibits a drop in accuracy for all classes. However, layers 9 to 31 (at at the end of forth and fifth convolutional layers), provide a high accuracy, i.e. above 0.9 for all classes. These results indicate that a nine-layer architecture is appropriate for all classes. This specific architecture will be the considered in the sequel. Interestingly, the plot of the first two PCs dimensions (Fig. 7) exhibits a clearly distinctive class structure, with only a slight overlapping between neighboring classes. From the beginning of the magnetogram series ($\leq$ 2009, top-left) to its end ($\geq$ 2018, bottom-left), time follows a coherent horseshoe path, which is a pattern similar to the one found in Figs 6 and 10a. Future studies with more data from the next and subsequent solar cycles (from 25-th on) would allow to characterize the transition dynamics in the spaces of Figs 6, 10a, and 7, providing new tools to the analysis of solar phenomena.

The error distribution information shown in Fig. 11 reveals that classification error are concentrated on neighboring classes and with a time occurrence associated to the transition between classes. This is a consequence of the fact that we set sharp boundaries between classes while, in the physical process class transitions are gradual and with local variations within global trends.

The k-Means [19] and the GMM clustering algorithms, introduced in Section VI-B, are run on a random subsample of the training dataset, where each class has an equal number of representatives. The results shown in Fig. 12 reveal that there is a good correspondence between the original classes and those found through clustering. The only exception is the cluster that should represent the *Rising* class, that contains a greater number of *High* samples.

VII. Conclusions

Space weather is an important hazard to modern society with potentially severe negative effects on technology and the economy. This phenomenon strongly depends on the Sun's magnetic activity, investigated here with machine and deep learning computational intelligence techniques. The structure of the synoptic magnetograms with the dMSSIM dissimilarity measure corresponds to a space of at most 6 dimensions. Clustering techniques identified two distinct high density regions corresponding to the initial and final stages of the solar cycle respectively, where magnetograms show more homogeneous and less intense activity, although of a different kind. An intermediate region associated to the middle phase of the cycle exists and shows a high magnetic intensity and variability in both space and time. Deep learning solutions based on CNNs produced highly accurate models that successfully identified the main stages of the solar cycle. Class and time distributions were in good agreement with unsupervised results and errors concentrated at class boundaries.

Computational intelligence approaches proved very effective for characterizing the solar magnetic field and provided valuable insights on its behavior, structure, variation and evolution along a solar cycle.

Acknowledgment

The work utilizes data obtained by the Global Oscillation Network Group (GONG) Program (https://gong.nso.edu), managed by the National Solar Observatory, which is operated by AURA, Inc. under a cooperative agreement with the National Science Foundation. The data were acquired by instruments operated by the Big Bear Solar Observatory, High Altitude Observatory, Learmonth Solar Observatory, Udaipur Solar Observatory, Instituto de Astrofísica de Canarias, and Cerro Tololo Interamerican Observatory.

References

[1] C. Alippi, S. Disabato, and M. Roveri. Moving convolutional neural networks to embedded systems: the alexnet and vgg-16 case. In *Proceedings of the 17th ACM/IEEE International Conference on Information Processing in Sensor Networks*, pages 212–223. IEEE Press, 2018.

[2] C. Cortes and V. Vapnik. Support-vector networks. *Machine learning*, 20(3):273–297, 1995.

[3] S. Disabato and M. Roveri. Reducing the computation load of convolutional neural networks through gate classification. In *2018 International Joint Conference on Neural Networks (IJCNN)*, pages 1–8. IEEE, 2018.

[4] A. Krizhevsky et al. Imagenet classification with deep convolutional neural networks. In *NIPS*, volume 1 of *NIPS '12*, pages 1097—-1105. Curran Associates Inc., 2012.

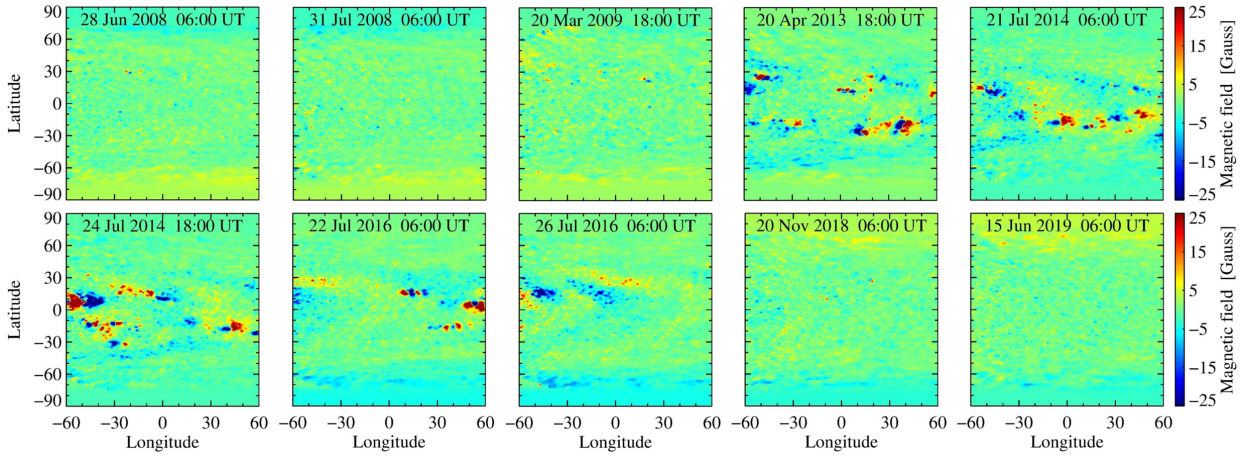

Fig. 8. Time sequence of Earth side magnetograms corresponding to the 10 medoids of Fig. 6 and Fig. 4b.

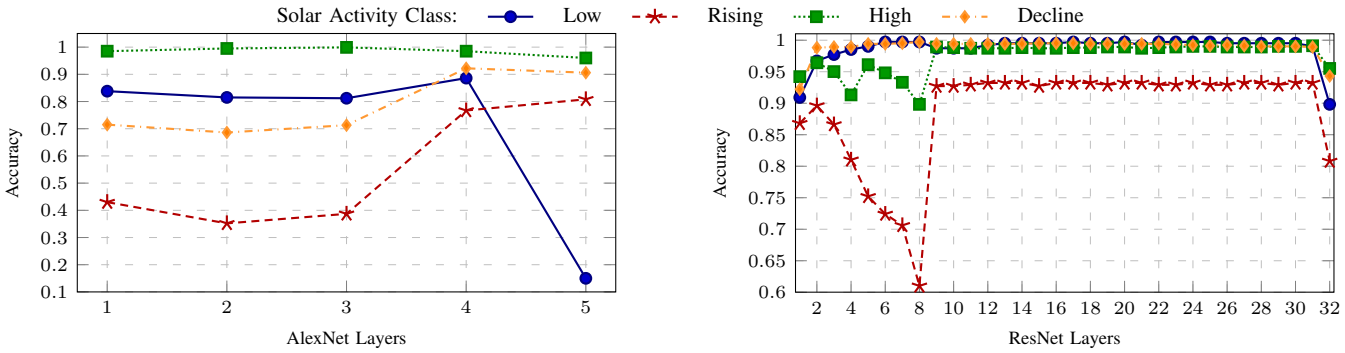

(a) SVM results on top of the AlexNet + PCA feature extractor.

(b) SVM results on top of the ResNet + PCA feature extractor.

Fig. 9. Accuracy of the AlexNet and ResNet CNNs using PCA feature spaces.

[5] H. He et al. Deep Residual Learning for Image Recognition. In *2016 IEEE Conference on Computer Vision and Pattern Recognition (CVPR)*, CPVR '16, pages 770–778. IEEE, jun 2016.

[6] J. Søgaard et al. Applicability of existing objective metrics of perceptual quality for adaptive video streaming. *Electronic Imaging*, 13:1–7, 2016.

[7] LeCun et al. Convolutional networks for images, speech, and time series. *The handbook of brain theory and neural networks*, 3361(10).

[8] M. Ankerst et al. Optics: ordering points to identify the clustering structure. *ACM SIGMOD*, 28(2):49–60, 1999.

[9] S. Wold et al. Principal component analysis. *Chemometrics and intelligent laboratory systems*, 2(1-3):37–52, 1987.

[10] Z. Wang et al. Image quality assessment: From error visibility to structural similarity. *IEEE Tran. on Image Processing*, 13(4), 2004.

[11] Zimek et. al. A survey on unsupervised outlier detection in high-dimensional numerical data. *Statistical Analysis and Data Mining: The ASA Data Science Journal*, 5(5):363–387, 2012.

[12] P. Grassberger and I. Procaccia. Measuring the strangeness of strange attractors. *Physica*, D(9):189–208, 1983.

[13] M. Hein and J.Y. Audibert. Intrinsic dimensionality estimation of submanifolds in euclidean space. In *Proc. ICML*, 2005.

[14] F. Hill. The Global Oscillation Network Group facility: An example of research to operations in space weather. *Space Weather*, 16(10):1488–1497, 2018.

[15] G.E. Hinton and S.T. Roweis. Stochastic neighbor embedding. *In Advances in Neural Information Processing Systems*, 15:833–840, 2002.

[16] L. Kaufmann and P. Rousseeuw. Clustering by means of medoids. In Y. Dodge, editor, *Statistical Data Analysis Based on the L_1–Norm and Related Methods*, pages 405—-416, 1987.

[17] E. Levina and P.J. Bickel. Maximum likelihood estimation of intrinsic dimension. *Advances in Neural Information Processing Systems*, 17:777–784, 2005.

[18] W Livingston, MJ Penn, and L Svalgaard. Decreasing sunspot magnetic fields explain unique 10.7 cm radio flux. *The Astrophysical Journal Letters*, 757(1):L8, 2012.

[19] Stuart Lloyd. Least squares quantization in pcm. *IEEE transactions on information theory*, 28(2):129–137, 1982.

[20] L. Nikolić. Modelling the magnetic field of the solar corona with potential-field source-surface and Schatten current sheet models. *Geological Survey of Canada, Open File*, 8007, 2017.

[21] L. Nikolić. On solutions of the PFSS model with GONG synoptic maps for 2006–2018. *Space Weather*, 17(8):1293–1311, 2019.

[22] G. J. D. Petrie. Solar magnetism in the polar regions. *Living Reviews in Solar Physics*, 12(1):5, Nov 2015.

[23] J. Pomoell and S. Poedts. EUHFORIA: European heliospheric forecasting information asset. *J. Space Weather Space Clim.*, 8:A35, 2018.

[24] J.W. Sammon. A nonlinear mapping for data structure analysis. *IEEE Transactions on Computers*, C-18(5):401—409, 1969.

[25] E. Schubert and M. Gertz. Improving the cluster structure extracted from optics plots. In *Proc. of Lernen, Wissen, Daten, Analysen (LWDA)*, pages 318–329, 2018.

[26] H. Schwabe and H. H. Schwabe. Sonnen — beobachtungen im jahre 1843. *Astronomische Nachrichten*, 21(15):234–235, 1844.

[27] R. A. Steenburgh, D. A. Biesecker, and G. H. Millward. From predicting solar activity to forecasting space weather: Practical examples of research-to-operations and operations-to-research. *Solar Physics*, 289(2):675–690, 2014.

[28] X. Sun, Y. Liu, J. T. Hoeksema, K. Hayashi, and X. Zhao. A new method for polar field interpolation. *Solar Physics*, 270(1):9–22, 2011.

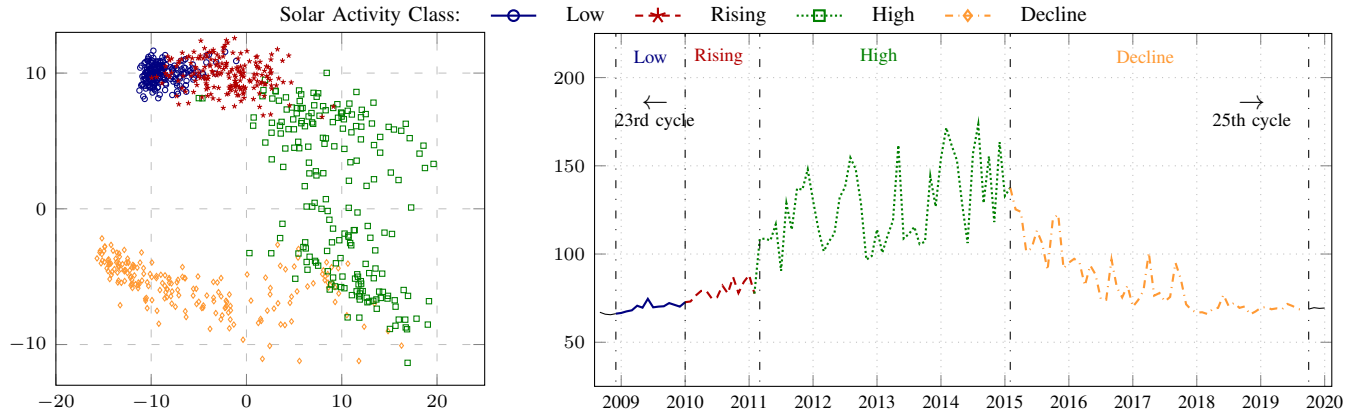

(a) Object distribution the feature space.

(b) Classes distribution with time, overlaid on the adjusted 10.7cm solar flux.

Fig. 10. Class definition according to solar activity (right) and the distribution in the first two feature space PCs (*conv4_0* layer of the ResNet CNN.

Real Class \ Predicted Class	Low	Rising	High	Decline
Low	389	5	0	0
Rising	24	366	5	0
High	0	13	1413	3
Decline	0	0	10	1729

(a) Confusion matrix of the Gaussian SVM.

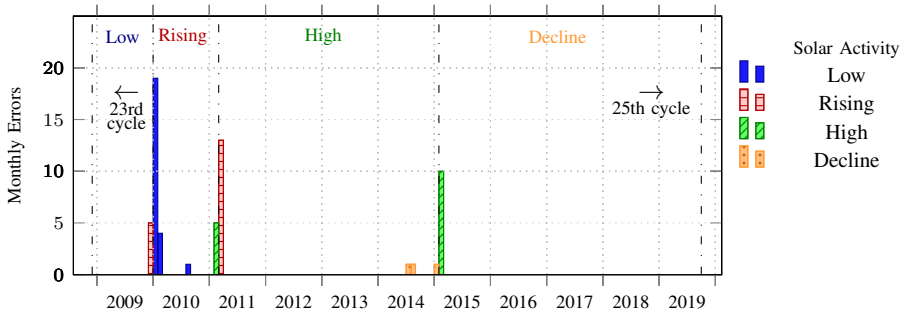

(b) Error distribution with time. For each month the number of errors is plotted.

Fig. 11. Gaussian SVM classification results on the features space defined by the output of ResNet layer *conv4_0*, followed by a 3468 PCs (containing 95% of the variance). Right: Confusion matrix. Left: Error distribution with time. Note that almost all the errors are close to class transitions.

	Cluster	Real Class: Low	Rising	High	Decline
k-Means (b)	○	**395**	165	4	0
	★	5	288	**420**	0
	□	0	0	**1011**	329
	◇	0	0	2	**1337**
GMM (c)	○	**388**	115	2	0
	★	12	338	**383**	0
	□	0	0	**1049**	318
	◇	0	0	3	**1348**

(a) Training sample distribution in the clusters.

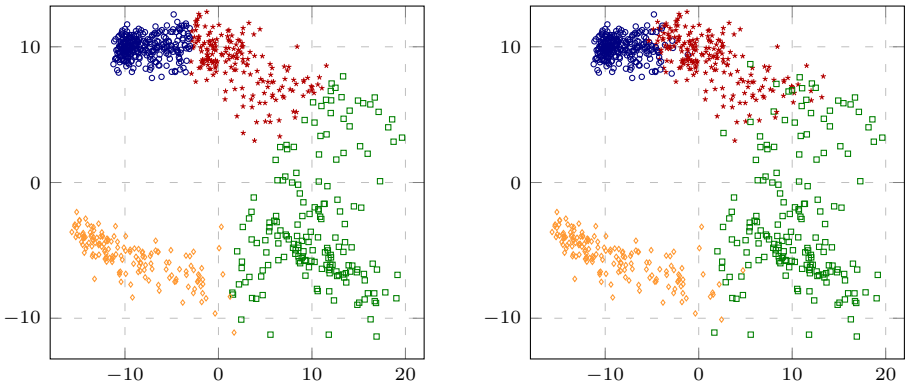

(b) k-Means results.

(c) GMM results.

Fig. 12. Clustering the deep learning two PCs feature space: (a) Comparison of cluster memberships with actual class composition. (b) k-Means results. (c) GMM results.

[29] Gábor Tóth, Bart van der Holst, and Zhenguang Huang. Obtaining potential field solutions with spherical harmonics and finite differences. *The Astrophysical Journal*, 732(2):102, 2011.

[30] G. Trunk. Statistical estimation of the intrinsic dimensionality of a noisy signal collection. *IEEE Trans. on Computers*, 25:165—-171, 1976.

[31] J. J. Valdés, L. Nikolić, and K. Tapping. Machine learning approaches for predicting the 10.7 cm radio flux from solar magnetogram data. In *2019 International Joint Conference on Neural Networks (IJCNN)*, pages 1–8. IEEE, 2019.

[32] P. J. Verveer and R. Duin. An evaluation of intrinsic dimensionality estimators. *IEEE Transaction on Pattern Analysis and Machine Intelligence*, 17(1):81—-86, 1995.

[33] J. Yosinski, J. Clune, Y. Bengio, and H. Lipson. How transferable are features in deep neural networks? In *Advances in neural information processing systems*, pages 3320–3328, 2014.

[34] L. Zhang, L. Zhang, and X. Mouand D. Zhang. A comprehensive evaluation of full reference image quality assessment algorithms. In *Proc. 19th IEEE International Conference on Image Processing*, pages 1477—-1480, 2012.